Research Square

Preprints are preliminary reports that have not undergone peer review.
They should not be considered conclusive, used to inform clinical practice,
or referenced by the media as validated information.

Performance of C24N24 Single Atom Catalysts for Methane Oxidation: A Combined QTAIM, IBO and DIAS Analysis

Kwanele C. Ngubane
University of Johannesburg
Mafereka F.T. Moabisane
University of the Free State, (Qwaqwa Campus)
Adedapo S. Adeyinka
aadeyinka@uj.ac.za

University of Johannesburg

Research Article

Keywords: Methane Oxidation, Transition metal, Single-atom catalyst, Fullerene, Activation Energy

Posted Date: May 12th, 2026

DOI: https://doi.org/10.21203/rs.3.rs-9436195/v1

License: This work is licensed under a Creative Commons Attribution 4.0 International License.
Read Full License

Additional Declarations: No competing interests reported.

Performance of $C_{24}N_{24}$ Single Atom Catalysts for Methane Oxidation: A Combined QTAIM, IBO and DIAS Analysis

Kwanele C. Ngubane[a], Mafereka F.T. Moabisane[b], and Adedapo S. Adeyinka [a]*

[a] *Research Centre for Synthesis and Catalysis (RCSC), Department of Chemical Sciences, University of Johannesburg, PO Box 524, Auckland Park, 2006, Johannesburg, South Africa.*

[b] *Department of Chemistry, University of the Free State, (Qwaqwa Campus), Phuthaditjhaba, South Africa.*

Corresponding author: Adedapo S. Adeyinka (aadeyinka@uj.ac.za)

Abstract

The direct, efficient and selective oxidation of methane to methanol remains a major challenge in catalysis due to the strength of the C–H bond and the tendency for overoxidation. This study investigates the catalytic potential of first-row (Mn, Fe, Co, Ni, Cu) and second-row (Ru, Rh, Pd) transition metals as single-atom catalysts (SACs) supported on nitrogen-doped fullerene ($C_{24}N_{24}$) for methane oxidation to methanol. Using Density Functional Theory (DFT) calculations, we calculated the activation barriers for each metal-doped system. Further analysis using the DIAS model, QTAIM, and IBO theory provided insight into the geometric, electronic, and orbital factors that influence the catalytic activity of SACs for methane activation. The results reveal that Ni and Cu SACs have the lowest activation barriers due to negligible structural distortion and more negative interaction energies at the transition state. QTAIM analysis revealed significant differences in bond critical point features of various TM-O interactions, whereas IBO analysis demonstrated that more efficient catalysts promote smoother and more delocalized electron rearrangements during C-H activation. Metals, such as Ru and Mn, exhibit increased electron localization and structural reorganization, which corresponds to higher energy barriers. This emphasises the importance of structural, electrostatic, and orbital parameters in determining the catalytic performance of SACs for methane oxidation. The findings help rationalize the design of effective methane valorisation $C_{24}N_{24}$ supported SACs and provide useful methodologies for modifying their selectivity and activity using atomic-level changes.

Keywords

Methane Oxidation, Transition metal, Single-atom catalyst, Fullerene, Activation Energy

1. Introduction

Methane is an abundant carbon resource, making it a major contributor to greenhouse gas emissions as a natural gas.[1,2] The conversion of methane to methanol is highly desirable as methanol is currently increasing on the market due to its wide use.[3,4] Methanol in particular is used in fuel, chemical synthesis, and energy storage.[5-8] Therefore, reducing this natural gas, which contributes to greenhouse gas emissions, while meeting demand for renewable energy

sources (such as methanol) is significant.[9] The catalysts are essential because they facilitate the activation of C–H bonds, which increases methane reactivity under relatively moderate conditions and promotes faster reaction kinetics, such as the methane conversion process.[10,11,12] However, the exceptional stability of C-H in methane[13] and the high susceptibility of methanol to over-oxidation result in undesired by-products such as CO_2, formaldehyde, making the selective oxidation of methane to methanol a long-standing challenge.[14] To overcome these challenges, a significant effort by researchers has gone into creating sophisticated catalyst systems that can activate methane under moderate conditions while inhibiting over-oxidation pathways to get beyond these basic restrictions.

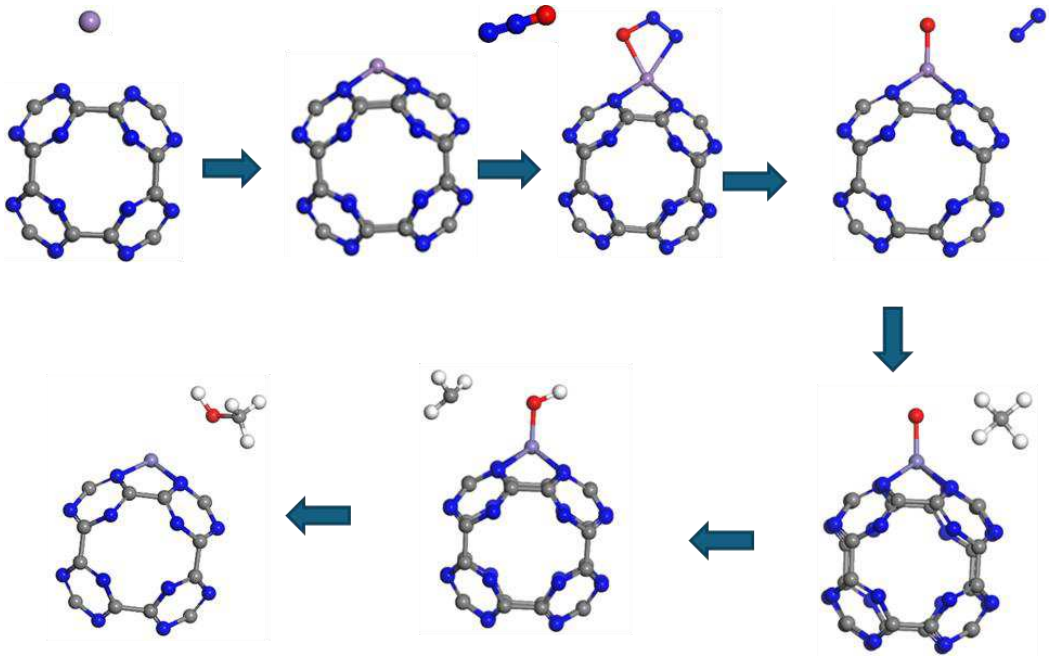
In recent years, heterogeneous catalysts have emerged as a viable approach for facilitating methane activation under milder conditions.[15,16] Transition metal catalysts have demonstrated a significant activity in C-H bond activation and selective oxidation, particularly those based on 2nd–row transition metals such as Ru, Rh, and Pd.[17,18] However, low atom utilization efficiency, poor control over active-site uniformity, limited product selectivity due to ensemble effects, and catalyst deactivation from sintering or coke formation under harsh reaction conditions are just a few of the inherent problems that conventional heterogeneous catalysts frequently face.[19] Furthermore, the large-scale industrial use of noble metals is severely hampered by their limited natural availability and high cost. These limitations have driven interest in finding cost-effective alternatives that are more earth-abundant and easily accessible, with potential catalytic performance equivalent to that of conventional catalysts. Due to their high metal-atom efficiency, well-defined active sites, and distinctive electronic properties, single-atom catalysts (SACs) have recently attracted significant attention amid the performance and cost constraints of conventional heterogeneous catalysts. [20,21]

Single-atom catalysts (SACs) have garnered considerable attention recently because of their capacity to optimize metal atoms and offer unique electronic structures that distinguish them from bulk or nanoparticle catalysts.[22] In SAC systems, isolated metal atoms anchored to suitable supports exhibit well-defined active sites, precise, tunable electronic properties, and improved catalytic activity. For the direct conversion of methane to methanol, several transition metals, including Fe, Cu, Ni, Co, Mn, Ru, Rh, and Pd, have been investigated as SACs. These metals are usually anchored on supports such as metal oxides[23], zeolites[13], and nitrogen-doped carbon frameworks [24, 25]. Among these SAC supports, the rich nitrogen-doped carbon frameworks have become one of the most promising support materials. A particular support material is a nitrogen-rich fullerene-like nanocage, $C_{24}N_{24}$, which provides well-defined nitrogen sites that enable strong metal-support interactions and effectively stabilize single transition-metal atoms against aggregation.[24] Despite the rapid development of SACs for methane activation, there are limited systematic comparisons between the catalytic activity of

1st-row and 2nd-row transition metals on the same support material. Significantly, although many studies show that 1st-row transition metals have promising catalytic performance when supported, little is known about the underlying factors that lead to their superior activity, or how their 2nd-row counterparts perform when supported on similar materials. For instance, Esrafili and Mousavian[26] and Zhang *et al*.[27] only compared the catalytic performance of 1st-row transition metals (Ti, V, Fe, Co, Ni) anchored on $C_{24}N_{24}$, with Ni demonstrating superior catalytic activity. Therefore, to develop a catalyst that is both low-cost and highly effective for converting methane to methanol, this knowledge gap must be addressed.

Hence, this study presents a thorough density functional theory (DFT) investigation and comparison of the catalytic activity of first- and second-row transition-metal atoms supported on $C_{24}N_{24}$ as SACs for the direct oxidation of methane to methanol. We evaluate the structural and electronic stability of the TM doped into $C_{24}N_{24}$ via binding energy calculations, HOMO-LUMO gap analysis, and density-of-states (DOS) analysis. We then simulate the entire catalytic cycle for the conversion of methane to methanol based on these stability evaluations, and we methodically evaluate the activation energy barriers for the crucial reaction stages across the metals under study. Furthermore, to understand the fundamental origin of the catalytic performance between first- and second-row transition metals, we integrate the activation strain model (ASM)[28,29], quantum theory of atoms in molecules (QTAIM)[30], and intrinsic bond orbital (IBO)[31,32] analysis to elucidate the interplay of the strain, electronic interactions, charge transfer, and orbital hybridization toward the activation energy barrier during the C-H bond activation.

2. Methodology



Scheme 1: Flowchart of all complexes involved in this reaction.

The $C_{24}N_{24}$, TM@$C_{24}N_{24}$ structures were geometry optimized by DMol^{3} [33] module implemented on Biovia Materials Studio 2020. The Perdew-Burke-Ernzerhof (PBE)[34,35] and double numeric plus polarization (DNP^{+})[33] basis set was utilized throughout all the calculations. The key oxo-metal intermediate (OTM@$C_{24}N_{24}$) was generated by adsorbing a nitrous oxide (N_2O) molecule onto the TM@$C_{24}N_{24}$ catalyst. By facilitating the transfer of an oxygen atom from N_2O to the transition metal centre, this adsorption creates the reactive oxo-metal species, which then combines with CH_3 to generate CH_3OH (Following the Scheme 1 shown above). The TS search and verification were performed using ORCA 6.0[36] with NEB-TS[37] method with PBE/def2-TVPP level of theory[38]. Further, IRC calculations were done to confirm the TS identified and reaction barriers.

To check the stability of TM on the $C_{24}N_{24}$ fullerene, the binding energies *(E_b)* were calculated as follows:

$$E_b = E_{(TM@C_{24}N_{24})} - E_{TM} - E_{C_{24}N_{24}} \quad \text{..... Eq.1}$$

Further, we gained a better understanding of the catalytic activity of the TM@$C_{24}N_{24}$ systems toward methane activation by employing a combination of analyses, namely the activation strain model, the quantum theory of atoms in molecules via the topology of the electron density, and intrinsic bonding orbital analysis.

3. Results and Discussion

3.1. Stability of TM on $C_{24}N_{24}$ of TM@$C_{24}N_{24}$

The geometric and electronic structure of $C_{24}N_{24}$ shows that this carbon nitride fullerene exhibits semiconductor characteristics as reported in previous $C_{24}N_{24}$ studies. This is demonstrated by a small energy gap between the valence and conduction bands, which allows easier electron transfer between the two bands, as displayed in Figure 1. The structural and electronic characteristics of the $C_{24}N_{24}$ system are considerably altered as the transition metals are introduced on the $C_{24}N_{24}$ fullerene, as indicated by the data in Figure 2 and Table 1. The thermodynamic stability of the TM@$C_{24}N_{24}$ clusters, as confirmed by the binding energy values shown in Figure 3, indicates that all TM atoms bond exothermically to the nitrogen anchoring site. The first-row transition metals (Mn, Fe, Co, Ni, and Cu) among the metals studied exhibit significantly stronger binding than the second-row metals (Ru, Rh, Pd). Specifically, Fe@$C_{24}N_{24}$ (-14.55 eV) and Mn@$C_{24}N_{24}$ (-12.16eV) exhibit the maximum stability on the support due to their largest negative binding energies. Their lower charge densities and larger ionic radii enable enhanced interaction between the N-2p orbitals of $C_{24}N_{24}$, leading to stronger contact. On the other hand, possibly larger atomic diameters and more diffuse orbitals of Ru,

Rh, and Pd exhibit less interaction. First row metals such as Co, Ni, and Cu binding strengths on the system are closer to the optimal region that the Sabatier principle predicts. This balance indicates that they are robust enough to maintain a stable anchor while still enabling effective cycles of reactant and product adsorption and desorption. As a result, it is anticipated that they should be better catalytic on $C_{24}N_{24}$. The TM adsorption significantly changes the electronic structure of $C_{24}N_{24}$ from the standpoint of reactivity – see Figure 4. In comparison to the pristine system, the HOMO-LUMO gap narrows by 30-65%, indicating improved charge transfer capacity and increased electronic reactivity. Furthermore, the PDOS analysis confirms a high degree of hybridization between the TM 3d/4d orbitals and the N-2p states, indicating the formation of a stable aggregate. Overall, most of the first-row transition metals are more stable on the $C_{24}N_{24}$ support because of their ideal balance between strong anchoring and advantageous catalytic reactivity based on the binding energy, electronic structural alterations, and the Sabatier principle.

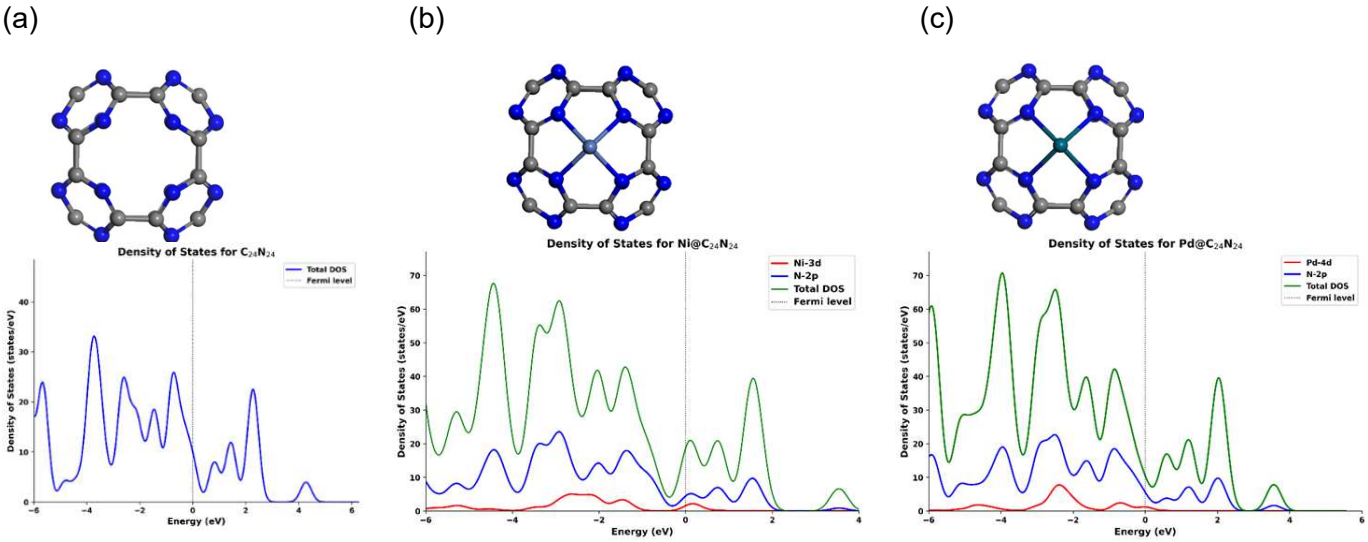
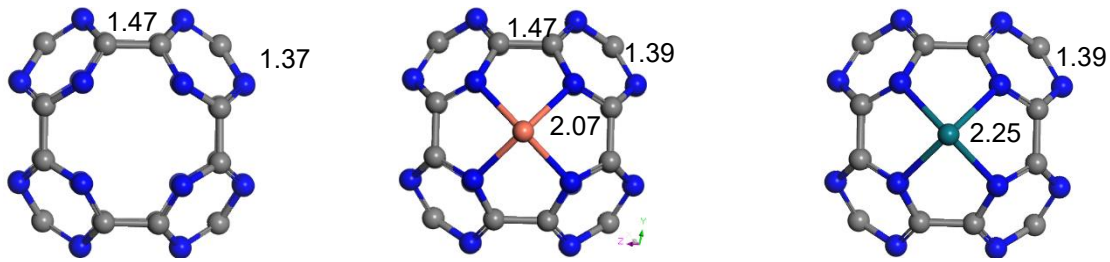


Figure 1: The density of state of bare $C_{24}N_{24}$ and TM@$C_{24}N_{24}$ systems



(a) Bare $C_{24}N_{24}$ (b) Cu@$C_{24}N_{24}$ (c) Rh@$C_{24}N_{24}$

Figure 2: Geometric structure of (a) Bare $C_{24}N_{24}$, and TM@$C_{24}N_{24}$ (b)-(c)

Table 1: Calculated bond lengths (Å) and binding energy (eV) of transition metals on the $C_{24}N_{24}$ fullerene.

System	Binding Energy (eV)	TM-N (Å)	C-C (Å)	C-N (Å)
$C_{24}N_{24}$	-	-	1.468	1.367
$Mn@C_{24}N_{24}$	-12.16	2.031	1.466	1.396
$Fe@C_{24}N_{24}$	-14.55	2.011	1.465	1.394
$Co@C_{24}N_{24}$	-11.17	2.017	1.463	1.391
$Ni@C_{24}N_{24}$	-9.10	2.040	1.464	1.389
$Cu@C_{24}N_{24}$	-6.31	2.074	1.465	1.387
$Ru@C_{24}N_{24}$	-1.89	2.194	1.464	1.391
$Rh@C_{24}N_{24}$	-1.89	2.250	1.465	1.385
$Pd@C_{24}N_{24}$	-0.66	2.365	1.466	1.386

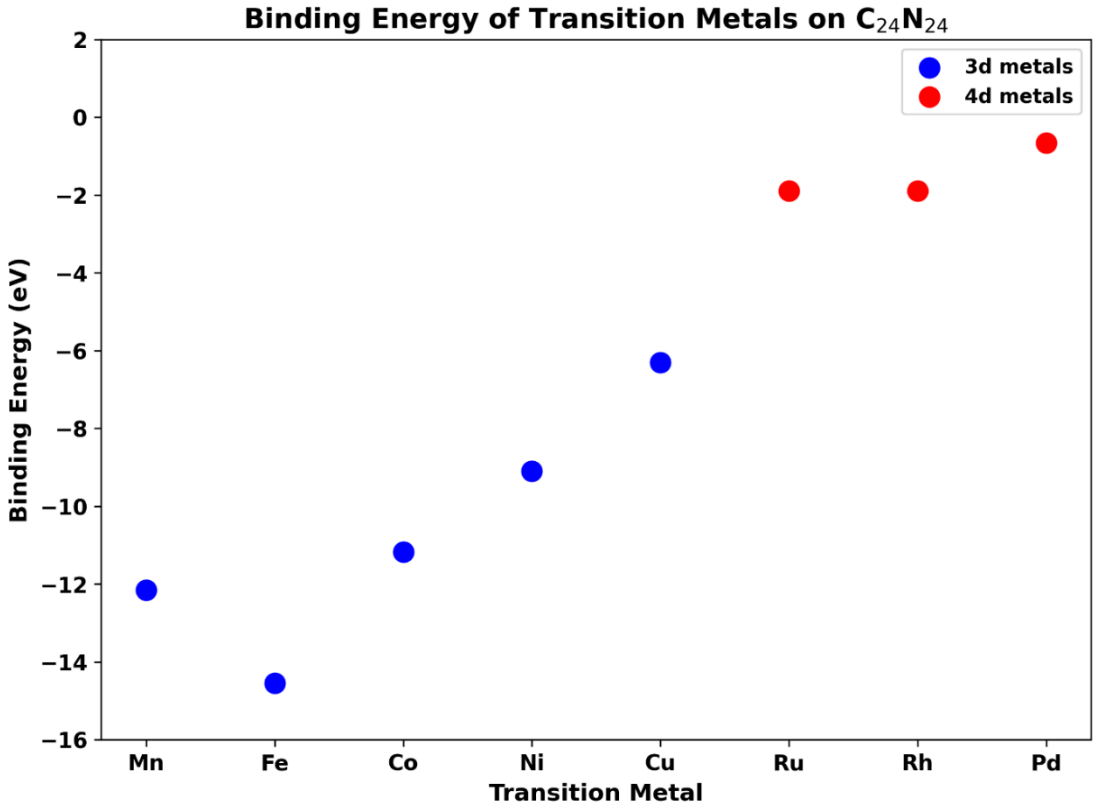


Figure 3: The binding energies vs d-blocks of transition metals on the $C_{24}N_{24}$ plot.

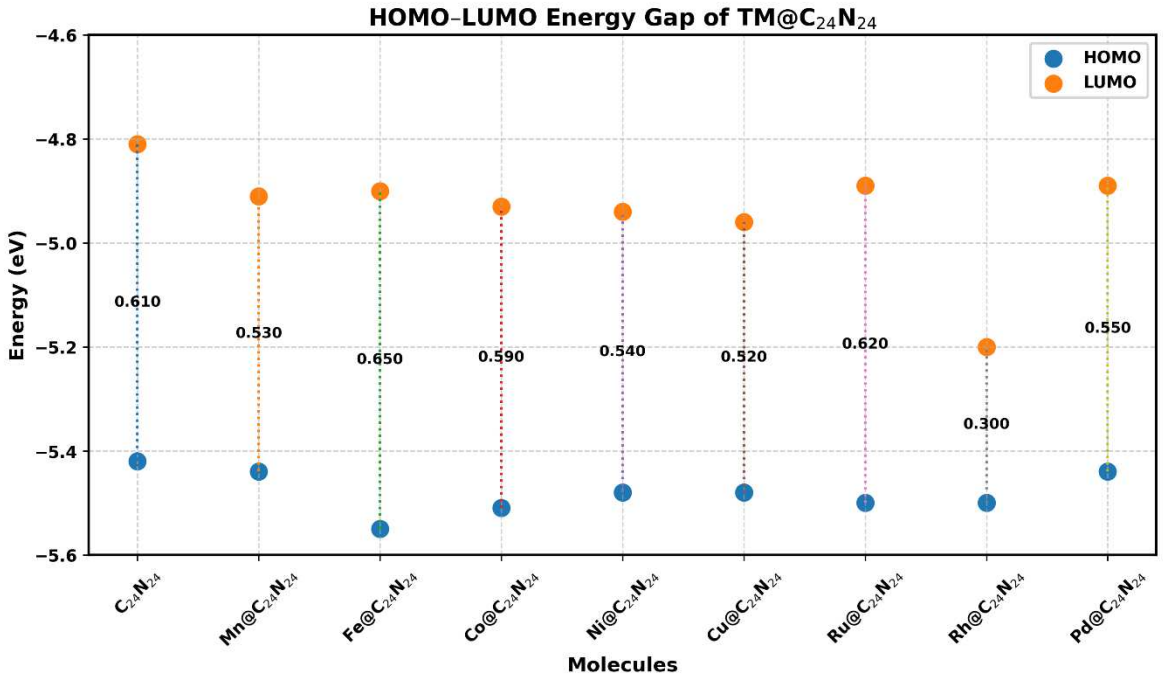
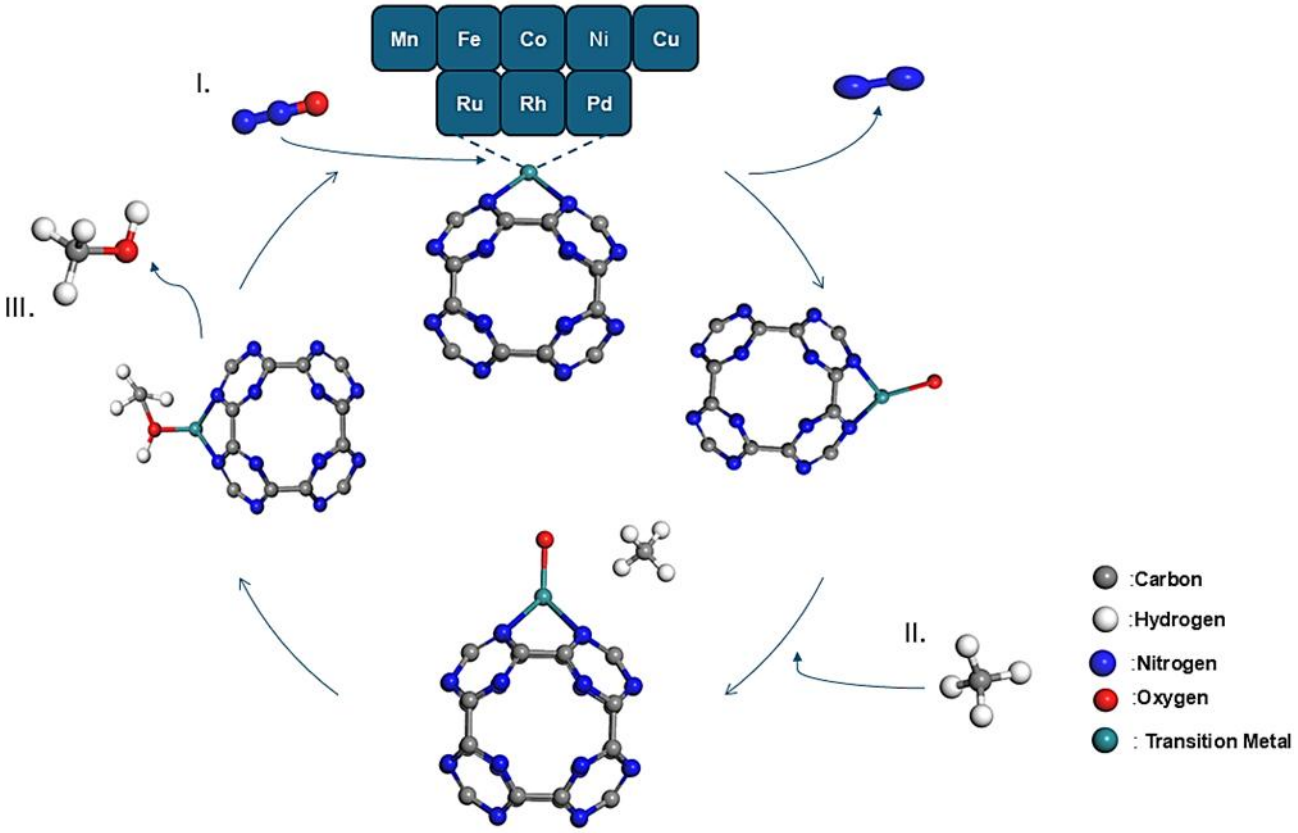


Figure 4: HOMO-LUMO Energy Gap of TM-doped $C_{24}N_{24}$.

3.2. The CH_4 Oxidation reaction in the presence of $TM@C_{24}N_{24}$ Single-Atom Catalyst



Scheme 2: Modelled catalytic cycle for methane-to-methanol in the presence of $OTM@C_{24}N_{24}$

The reaction pathway shown in Figure 5 confirmed the following stepwise mechanism: 1. Initial physical adsorption of CH_4 on OTM@$C_{24}N_{24}$ intermediate, 2. The C-H bond elongation and cleavage to form CH_3 * and H, hydrogen forming OH with the adsorbed O from the OTM@$C_{24}N_{24}$ intermediate. Subsequently, a bond is formed between OH and CH_3^* to yield CH_3OH. The Gibbs free energies (ΔG, eV) shown in Table 2 for the principal O–TM@$C_{24}N_{24}$ intermediates are as follows: OMn@$C_{24}N_{24}$ (-0.03), OFe@$C_{24}N_{24}$ (3.21), OCo@$C_{24}N_{24}$ (-1.44), ONi@$C_{24}N_{24}$ (-3.05), OCu@$C_{24}N_{24}$ (-2.41), ORu@$C_{24}N_{24}$ (0.67), ORh@$C_{24}N_{24}$ (-1.33), and OPd@$C_{24}N_{24}$ (-2.74). The Gibbs energies offer direct insight into the thermodynamic stability of the oxidized intermediates, significantly affecting both the activation of methane and the subsequent release of methanol. The Gibbs free energies of the O–TM@$C_{24}N_{24}$ intermediates demonstrate that most first-row transition-metal systems (Co, Ni, Cu) display thermodynamically advantageous (exergonic) tendencies for methanol synthesis, evidenced by their negative ΔG values (-1.44, -3.05, and 2.41 eV, respectively). Manganese exhibits a ΔG near zero (-0.03 eV), indicating a minimal thermodynamic driving force and reduced overall exergonicity. Conversely, most second-row metals exhibit endergonic characteristics, as indicated by their positive or less negative ΔG values, such as ORu@$C_{24}N_{24}$ (+0.67 eV) and the moderately exergonic albeit comparatively weaker values for Rh (-1.33 eV) and Pd (-2.74 eV) compared to Ni and Cu. This trend emphasizes the better thermodynamic favourability of first-row TM SACs over their second-row counterparts.

The activation barrier for methane oxidation over first-row metals is shown in Figure 6, decreasing in the following order: Mn > Fe > Co > Ni > Cu, with Ni and Cu exhibiting the lowest barriers, suggesting that methane oxidation can proceed at moderate temperatures. The results are comparable since the computed barriers for Ni@$C_{24}N_{24}$ and Co@$C_{24}N_{24}$ in this work match those reported in previous DFT research.[26,27] Then, for the second row transition metals having the largest activation barrier compared to their fourth period counterparts, grouped as follows: Ru > Pd > Rh. Overall, the findings show that for the conversion of methane to methanol on $C_{24}N_{24}$, first-row transition metals perform better than their second-row counterparts as SACs. Ni@$C_{24}N_{24}$ and Cu@$C_{24}N_{24}$ stand out as the most promising SACs due to their low activation barriers, favourable reaction energetics, and weak methanol adsorption, which facilitate efficient product desorption.

Table 2: Calculated reaction barrier (E_{barr}(eV)), Gibbs energy (ΔG (eV)), and Hirshfeld charge on (Q_O(|e|)) for chemical reactivity of O_{ads} on TM@$C_{24}N_{24}$

Intermediates	$\Delta G(eV)$	$E_{barr}(eV)$	$Q_O\ (\|e\|)$
OMn@$C_{24}N_{24}$	-0.03	2.08	-0.278
OFe@$C_{24}N_{24}$	3.21	1.29	-0.243
OCo@$C_{24}N_{24}$	-1.44	0.58	-0.220
ONi@$C_{24}N_{24}$	-3.05	0.36	-0.274
OCu@$C_{24}N_{24}$	-2.41	0.36	-0.283
ORu@$C_{24}N_{24}$	0.67	2.10	-0.185
ORh@$C_{24}N_{24}$	-1.33	0.59	-0.289
OPd@$C_{24}N_{24}$	-2.74	0.86	-0.377

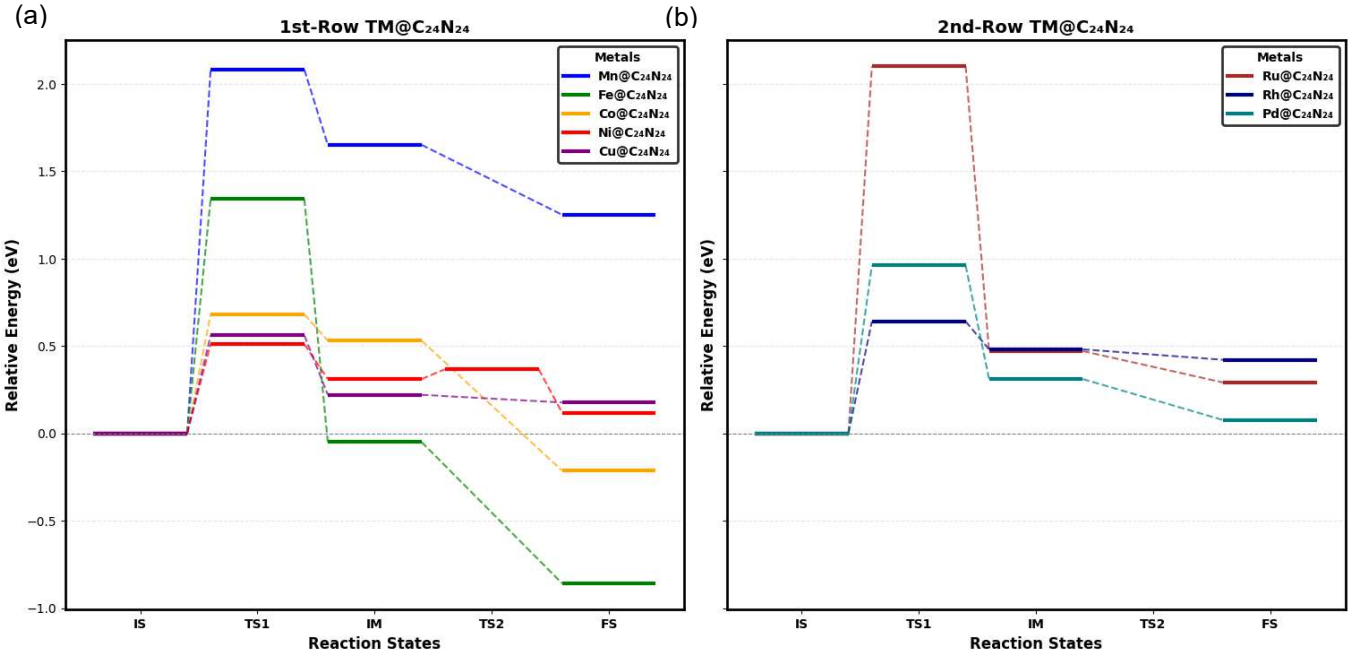


Figure 5: (a)-(b) The energy profile of methane oxidation via TM@$C_{24}N_{24}$,

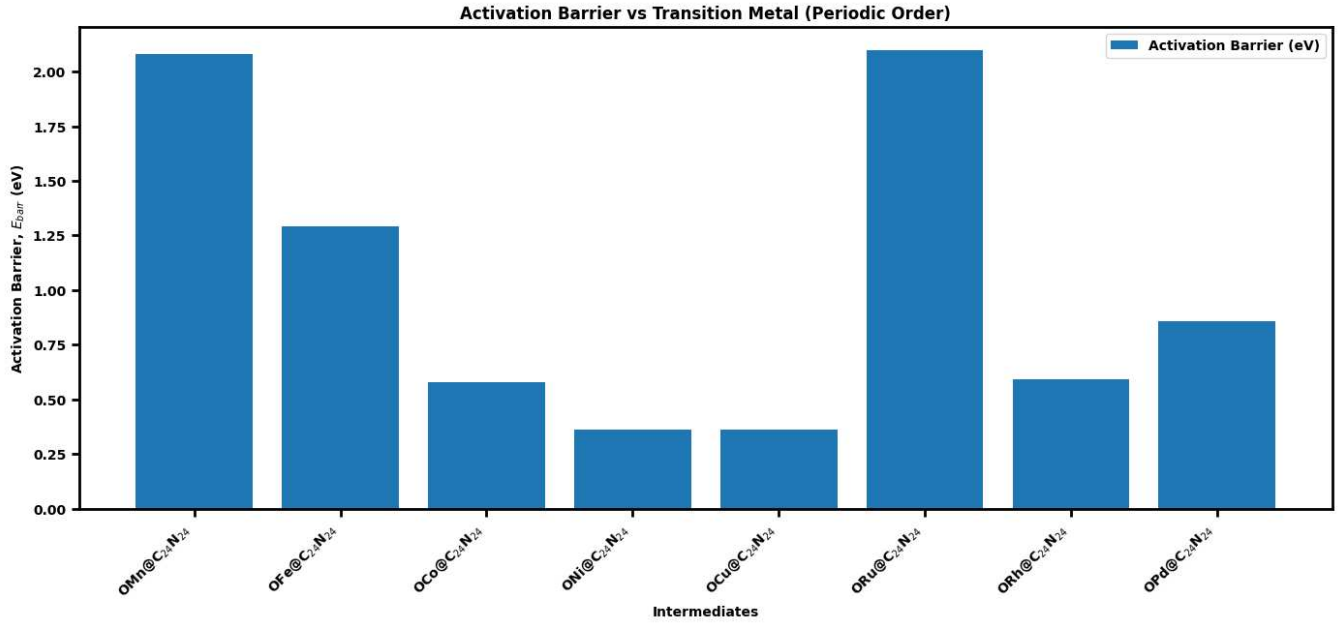


Figure 6: The activation barrier of methane oxidation comparison across the eight TMs.

3.3. A combined DIAS, QTAIM, and IBO Analysis of the Energy Barrier for Methane Oxidation using TM@$C_{24}N_{24}$ SACs.

3.3.1. Distortion/Interaction Activation Model

The Distortion/Interaction Activation Strain (DIAS) model was employed to investigate the factors influencing the activation barrier for the reaction. Within this framework, the activation energy is divided into the interaction energy between the two deformed fragments and the distortion energy, which is the energy needed to deform CH_4 and OTM@$C_{24}N_{24}$ from their ground-state geometries to their transition-state geometries. We can better understand how structural deformation and fragment interactions affect the overall barrier by analysing their contributions toward the reactivity. This method enables a more thorough understanding of how transition-metal doping affects reaction energetics. In this framework, the activation energy is decomposed into two main contributions: the distortion energy required to deform the reactants (CH_4 and OTM@$C_{24}N_{24}$) to their distorted geometries at the transition state, and the interaction energy between these distorted fragments.

Figure 7 shows the results of the DIAS analysis. Across all the transition metals, the energy required for CH_4 to distort from its relaxed geometry is consistently greater than that of the OTM@$C_{24}N_{24}$ fragment in systems, suggesting that deformation of methane is the primary cause of C-H bond activation. This also reveals the structural rearrangement required to weaken and break the C-H bond as hydrogen transfers to the adsorbed oxygen species. The total distortion energy ΔE_{dist}() follows the order: Ru > Fe > Mn > Pd > Co > Cu > Ni > Rh (0.58-3.28 eV), which is in good correlation with the reported activation barrier trend. This shows

that the degree of reactant complex distortion, as measured at TS in this work, largely determines reactivity, with systems requiring greater structural deformation exhibiting larger energy barriers. The interaction energies (ΔE_{int}), on the other hand, fluctuate over a rather narrow range (-42.50 to -37.30 eV), suggesting that interaction effects are less important than distortion. More stabilizing interactions with the deformed reactants are suggested by the somewhat higher negative interaction energies of first-row transition metals compared to second-row transition metals. These variations, however, are inadequate to offset significant distortion penalties in metals such as Fe and Ru, leading to larger activation barriers and later transition states. Because of its comparatively low distortion energies, Ni, Cu, and Rh can overcome deformation costs earlier along the reaction coordinate through stabilizing interactions. As a result, these systems exhibit reduced activation barriers and early transition states, thereby increasing catalytic activity. On the other hand, systems with higher distortion needs (such as Ru and Fe) exhibit lower reactivity because reconstructing the reactant complex incurs a higher energy cost.

Overall, these results show that the reactivity trend is dominated by the degree of distortion of the reactant complex, especially CH_4 deformation, and this correlates with catalytic activity. Catalysts that minimize structural reorganization during the transition state work better for C-H activation.

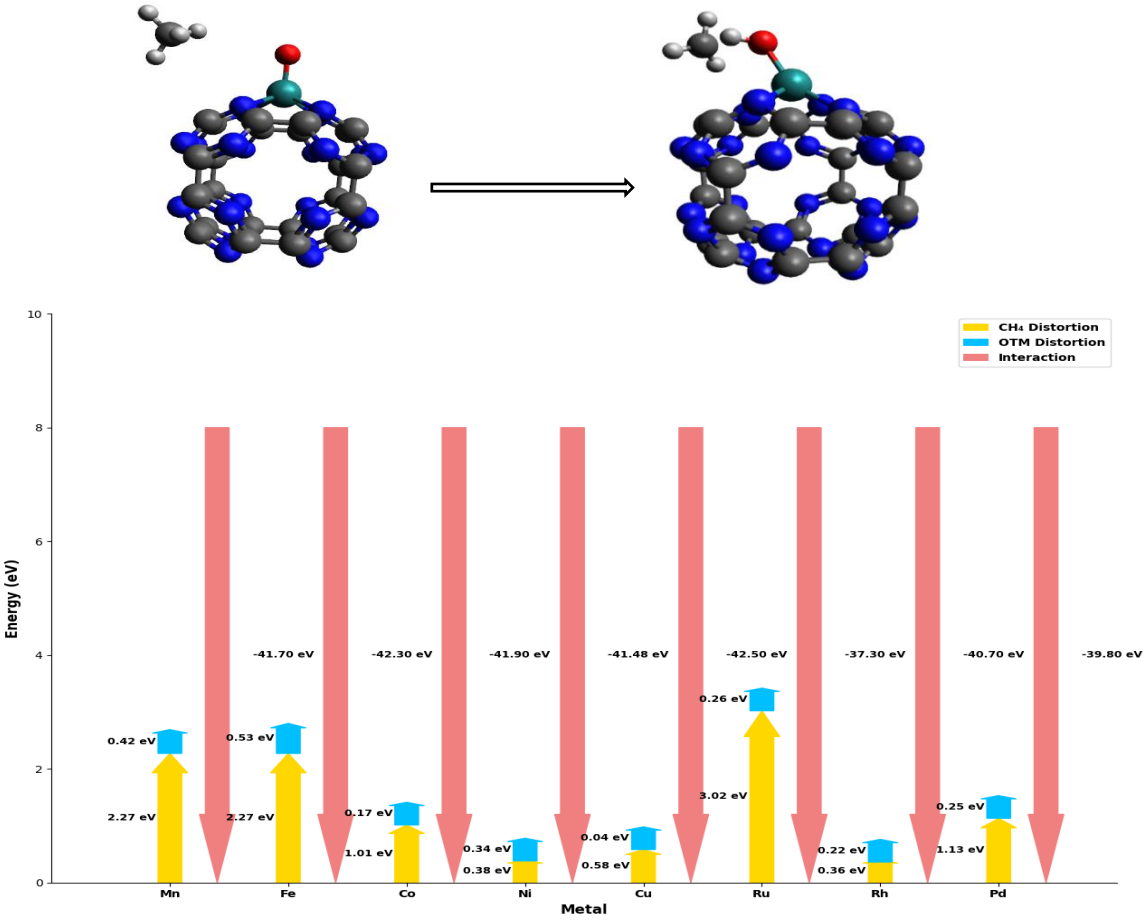


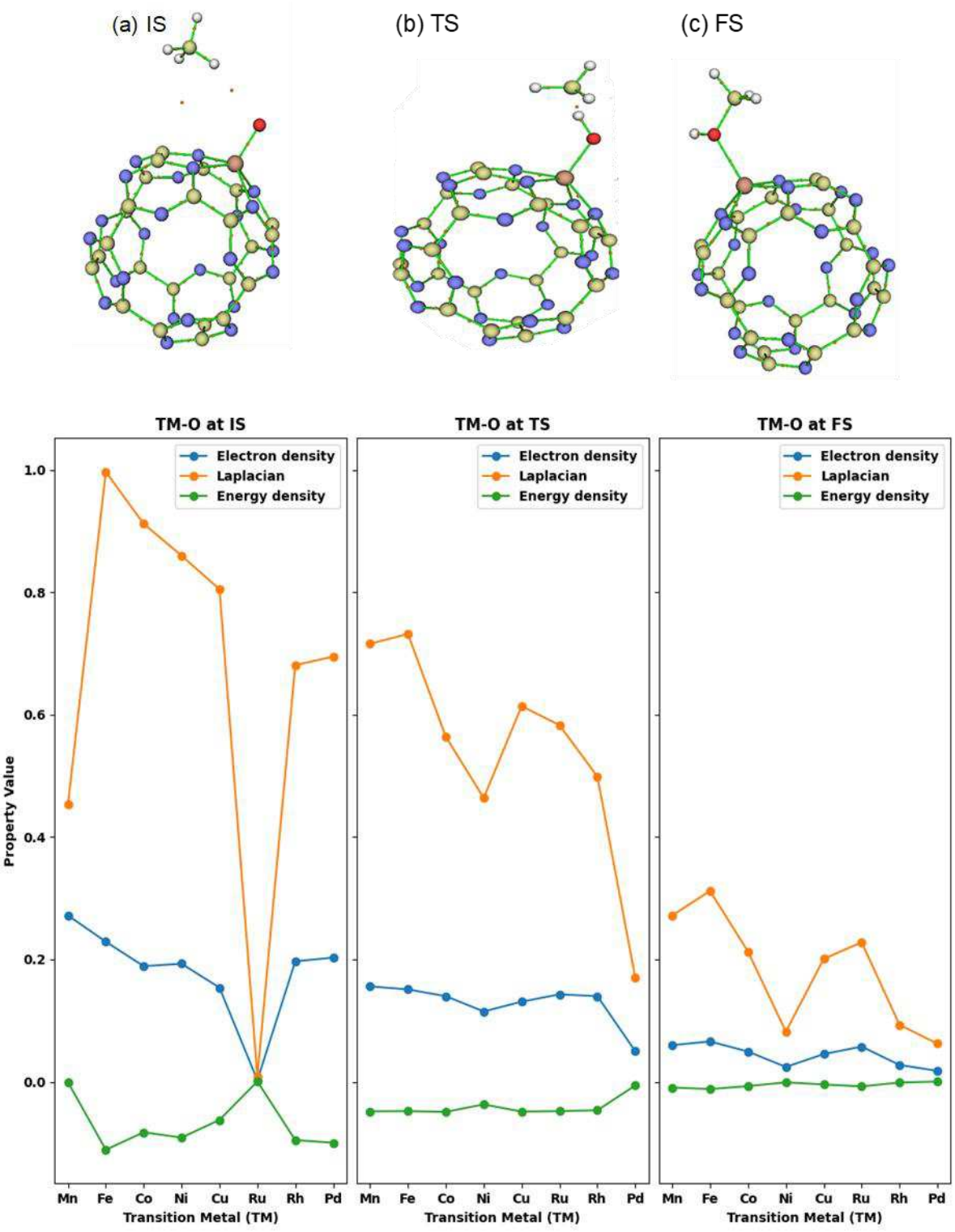
Figure 7: The DIAS plot with energy required for reactants, CH_4 (yellow) and $OTMC_{24}C_{24}$ (blue) to distort and interaction energy (red), TM = Mn/Fe/Co/Ni/Cu/Ru/Rh/Pd.

3.3.2. Quantum Theory Atom in a Molecule via Topology Analysis

The QTAIM analysis in Figure 8 further supports the mechanistic explanation provided by the DIAS analysis, by showing that these distortions are accompanied by bonding rearrangements. The electron density decreases, and the Laplacian becomes less positive along the reaction coordinate at the TM-O bond critical points (BCPs), signifying a steady weakening of the metal-oxo bond. The energy density becomes slightly positive at the final state in low-barrier systems like Ni and Cu, where this weakening is most noticeable. This suggests a weak or even somewhat destabilizing TM-O interaction that promotes methanol desorption. High-barrier systems (Mn, Fe, Ru, and Pd), on the other hand, have comparatively higher electron densities and more negative energy densities at TM-O BCPs, indicating stronger metal-oxo bonding and, thus, a greater energetic penalty for bond rearrangement during reaction. At the C-H BCPs, all the systems initially exhibit high electron density and strongly negative density, consistent with a strong covalent bond. The electron density at the C-H BCP drops as the reaction gets closer to the TS, signifying bond activation and cleavage. For Mn, Fe, Ru, and Pd, this reduction is more noticeable, indicating a more sophisticated C-

H bond-breaking process at their transition states. However, this substantial bond rearrangement results in higher energy costs and, consequently, larger activation barriers, as these systems also have strong TM-O bonds. While Ni, Cu, Co, and Rh exhibit greater electron density and more negative energy density at the C-H BCP near the TS, suggesting a less advanced but more energetically accessible C-H activation. Their reduced activation barriers and distortion energies are consistent with this characteristic. Strong C–O bond critical points (BCPs) in the final state are the final indication that methanol has been formed. The formation of a strong covalent bond is indicated by the high electron density and noticeably negative Laplacian at these locations. Early TM-O bond weakening and rupture in low-barrier single-atom catalyst systems enhance this transformation and encourage simpler product desorption.

When combined, these findings show that a careful balance between bond reconfiguration and reactant distortion controls catalytic activity. In addition to encouraging more gradual bond rearrangement and weaker TM–O contacts, catalysts like Ni and Cu reduce structural distortion and lower activation barriers. Mn, Fe, Ru, and Pd, on the other hand, undergo more significant structural and electrical reorganization and form stronger metal–oxo bonds, thereby increasing the distortion energy and activation barrier. Crucially, it is a trustworthy electronic indicator of methane activation reactivity since the degree of C–H bond activation is highly correlated with the decrease in electron density at the C–H BCP at the transition state.


(a) IS
(b) TS
(c) FS
TM-O at IS
TM-O at TS
TM-O at FS
Electron density
Laplacian
Energy density
Property Value
1.0
0.8
0.6
0.4
0.2
0.0
Mn
Fe
Co
Ni
Cu
Ru
Rh
Pd
Transition Metal (TM)

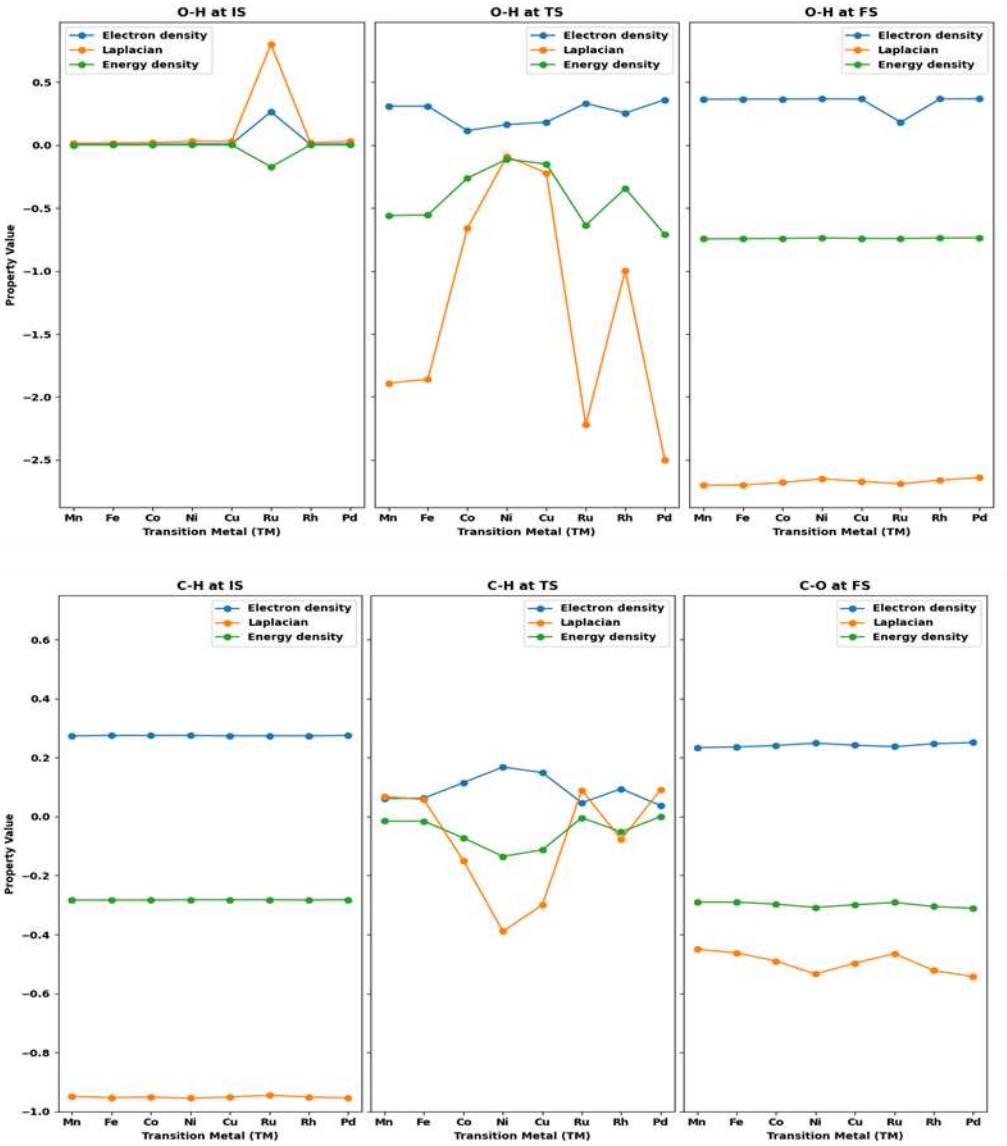


Figure 8: QTAIM topology analysis properties of (a) Reactant complex, (b) Transition state, (c) Product complex of the CH_4 into CH_3OH under the TM@$C_{24}N_{24}$ catalyst

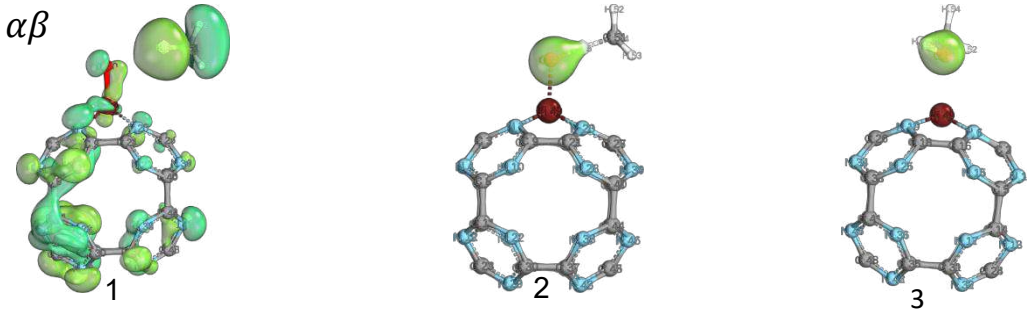
3.3.3. Intrinsic bonding orbital analysis

In addition to the DIAS and QTAIM analysis, the intrinsic bond orbital (IBO) analysis introduced by Knizia *et al.* was explored in this section to gain a deeper understanding of the energy barrier of the CH_4 activation process leading to methanol production. The bond-breaking and bond-formation mechanism was understood at the orbital level through an IBO study. A hydrogen atom transfer pathway involving homolytic C–H cleavage, in which one electron migrates with the H atom and the other stays on the CH_3 fragment, is confirmed by the IBOs (Figure 9, results for other metals are provided in the supplementary information) which clearly show how the σ(C–H) bond orbital changes into a σ(O–H) bond orbital throughout the process.

One electron from the initial C–H bond and one electron from the metal–oxo unit make up the newly created O–H bond.

The orbital energy study further supports these results. Ru has one of the highest activation barriers despite having the most negative (most stable) orbital energies along the reaction coordinate, as shown in Figure 10 (a). This suggests that significant orbital stability can raise the barrier by shifting the transition state later along the reaction coordinate and deepening the product well. Ni and Cu, on the other hand, exhibit lower orbital energy barriers and lower kinetic activation barriers due to their lower negative orbital energies and minor variations between IS and TS. Significant orbital energy differences along the reaction coordinate indicate substantial electronic rearrangement in metals like Mn and Fe, consistent with their higher activation barriers and distortion energies – see Figure 10 (b).

(a) $Ni@C_{24}N_{24}$



(b) $Ru@C_{24}N_{24}$

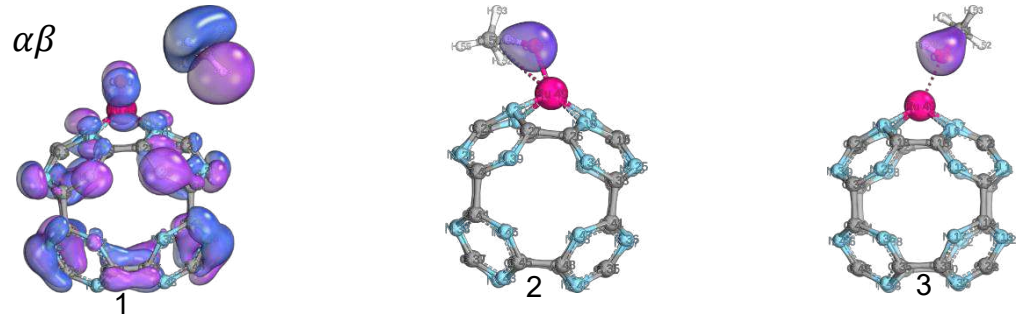


Figure 9: IBO analysis on 1. C-H bond at the initial state (IS), 2. TM-O-H bond at the transition state (TS) and 3. C-O-H bonds at the final state (FS).

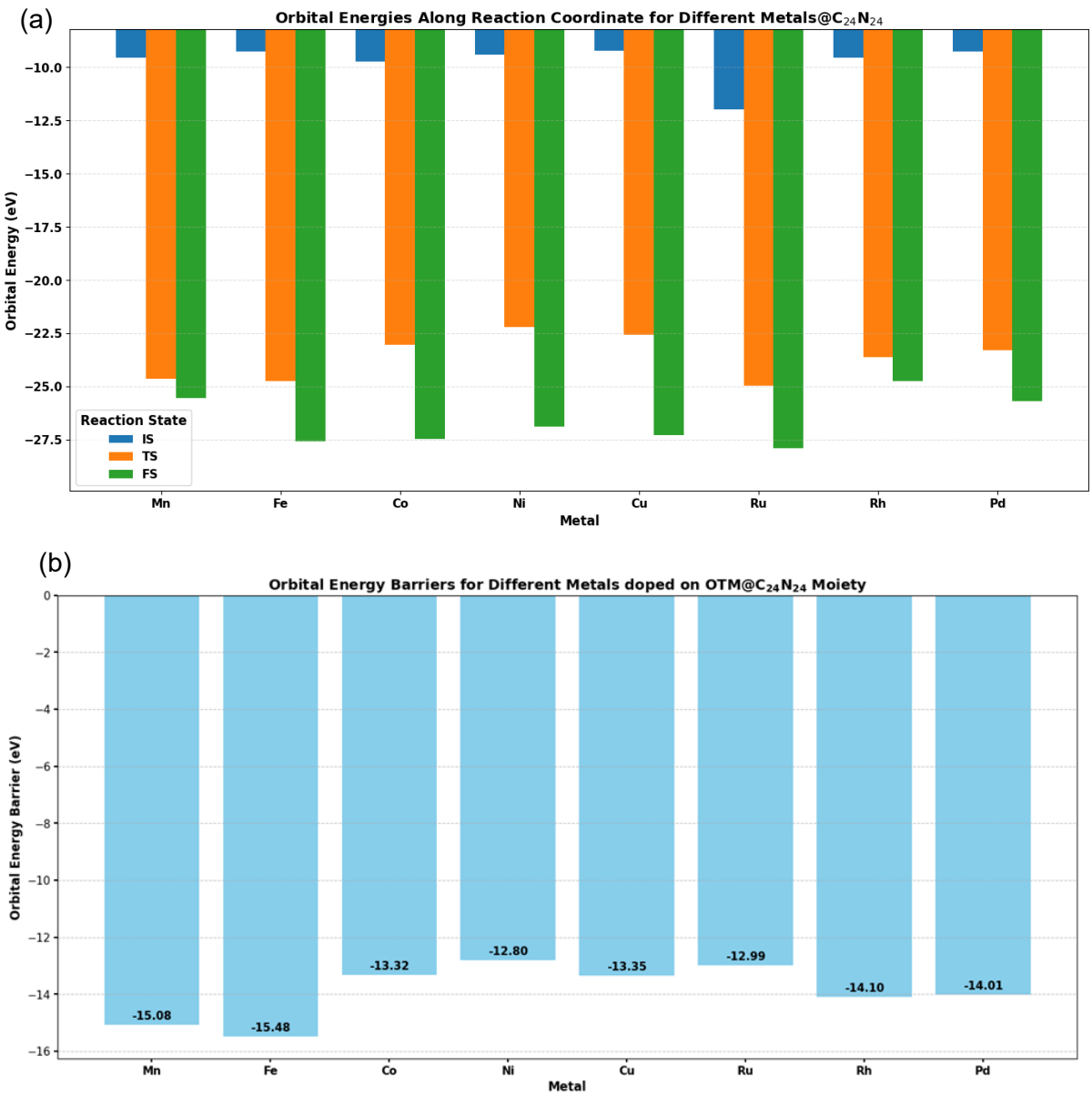


Figure 10: (a) Orbital energies of all TMs along the reaction and (b) Orbital energy difference (Orbital energy barrier from IS to TS) across the TM@$C_{24}N_{24}$ systems.

Overall, a careful balance between geometric distortion, bond critical point evolution, and orbital reorganization controls reactivity in methane activation over O–TM@$C_{24}N_{24}$, according to the combined DIAS, QTAIM, and IBO analyses. Lower activation barriers and more catalytic reactivity are shown in systems (such as Ni, Cu, and Rh) with weaker TM–O bonds, lesser CH_4 distortion, progressive C-H bond weakening, and mild orbital rearrangement. On the other hand, metals like Mn, Fe, Ru, and Pd that undergo significant bond rearrangement and form strong metal–oxo interactions incur higher energy costs, resulting in higher activation barriers and reduced reactivity.

3.4 Relationship correlation between the descriptors and activation barrier

The activation barrier and other electronic and structural characteristics were correlated using the Pearson correlation coefficient to determine the primary parameters controlling methane activation over OTM@$C_{24}N_{24}$ catalysts. Figure 11 is a heatmap showing correlations between all the various descriptors of catalytic activity examined and the activation energy.

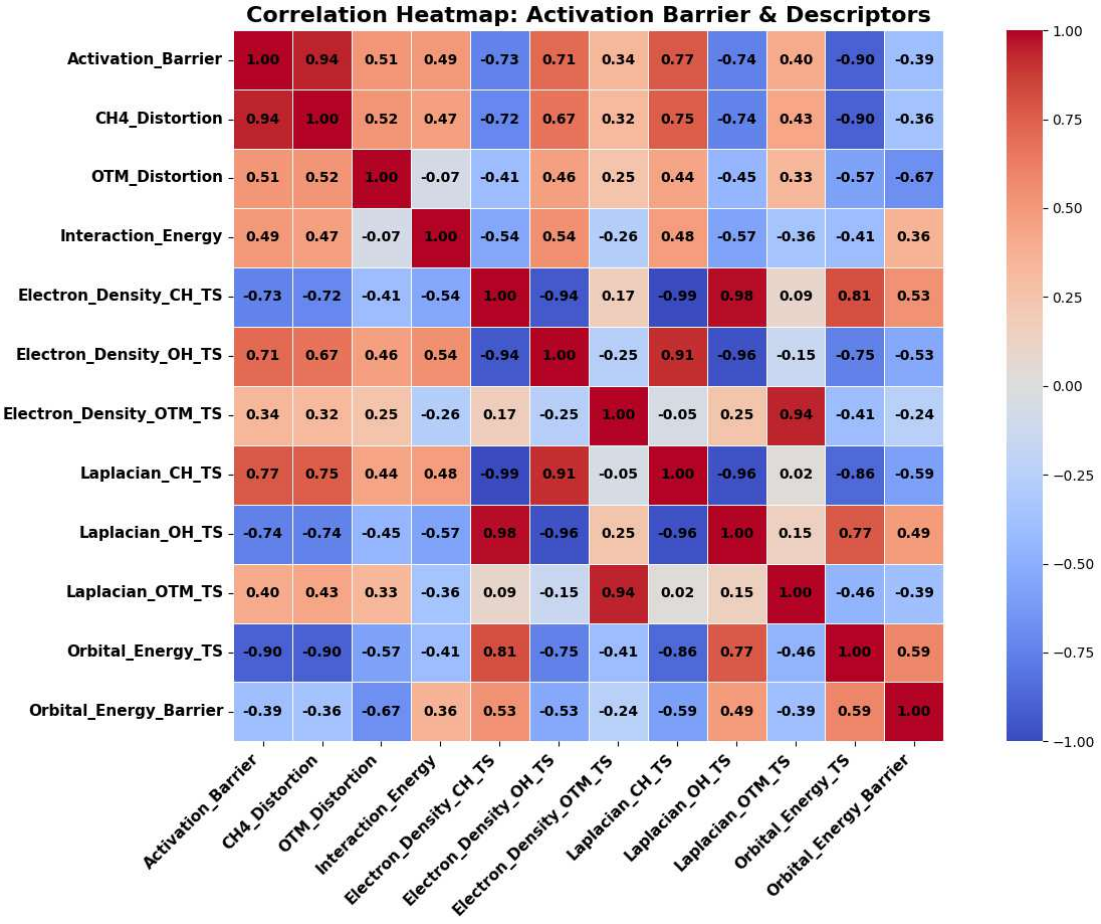


Figure 11: Correlation heat map highlighting the descriptors with more correlation to activation energy.

The most significant indicator of reactivity among the metrics examined is the CH_4 distortion energy at the transition state, which shows a remarkably strong positive correlation with the activation barrier ($r = 0.94$, $p < 0.05$). This suggests that systems with higher activation barriers require greater structural deformation of methane to reach the transition state. Therefore, the best method to lower the CH_4 activation barrier and increase catalytic activity is to minimize methane distortion. Additionally, there is a strong negative correlation between the activation barrier and the transition state orbital energy ($r = –0.90$, $p < 0.005$) – see Figure 12. This indicates that catalysts with lower negative TS orbital energies permit better electron reorganization during C–H bond breaking, resulting in lower activation barriers. Significantly,

there is a strong negative correlation (r = –0.90) between the TS orbital energy and the CH_4 distortion energy as shown in Figure 12, indicating an underlying relationship between structural strain and electronic reorganisation. These findings collectively demonstrate that the energy landscape of methane activation is jointly controlled by structural and electronic variables, with orbital energy serving as a secondary but essential descriptor and CH_4 distortion as the major driver.

According to the QTAIM perspective, there is a strong negative correlation ($r = –0.73$, $p < 0.05$) between the electron density at the C–H bond critical point (BCP) at the transition state and the activation barrier. This indicates that systems that maintain a higher electron density at the C–H bond in the TS have a lower energy barrier because the partially broken bond is better stabilized. On the other hand, greater activation barriers are correlated with stronger early O-H bond formation (seen by a larger electron density at the O-H BCP), suggesting that early product-like bonding raises the reaction's energy cost. However, the TM–O bond descriptors show modest relationships with the activation energy ($r < 0.4$), indicating that the metal–oxygen bond mainly serves as a supporting factor rather than actively regulating reactivity.

Overall, this multi-descriptor correlation analysis establishes a clear hierarchy of reactivity control, (i) The fundamental descriptor, CH_4 distortion energy on $TM@C_{24}N_{24}$, is the best indicator of both overall reactivity and the activation barrier, (ii) During C-H cleavage, electron rearrangement is controlled by transition-state orbital energy, a secondary descriptor and (iii) The effectiveness of C-H bond destabilization at the TS is reflected in the C-H BCP electron density, (iv) O–H and TM–O BCP characteristics are necessary but not the main ones. These results show that, rather than merely enhancing O–H or TM–O interactions, efficient methane activation over $TM@C_{24}N_{24}$ catalysts is mainly controlled by the catalyst's capacity to reduce methane distortion and promote gradual C–H bond weakening. Therefore, to achieve lower activation barriers and increased catalytic reactivity, catalyst systems that minimize CH_4 deformation and moderate orbital energy reorganisation should be prioritised in rational catalyst design.

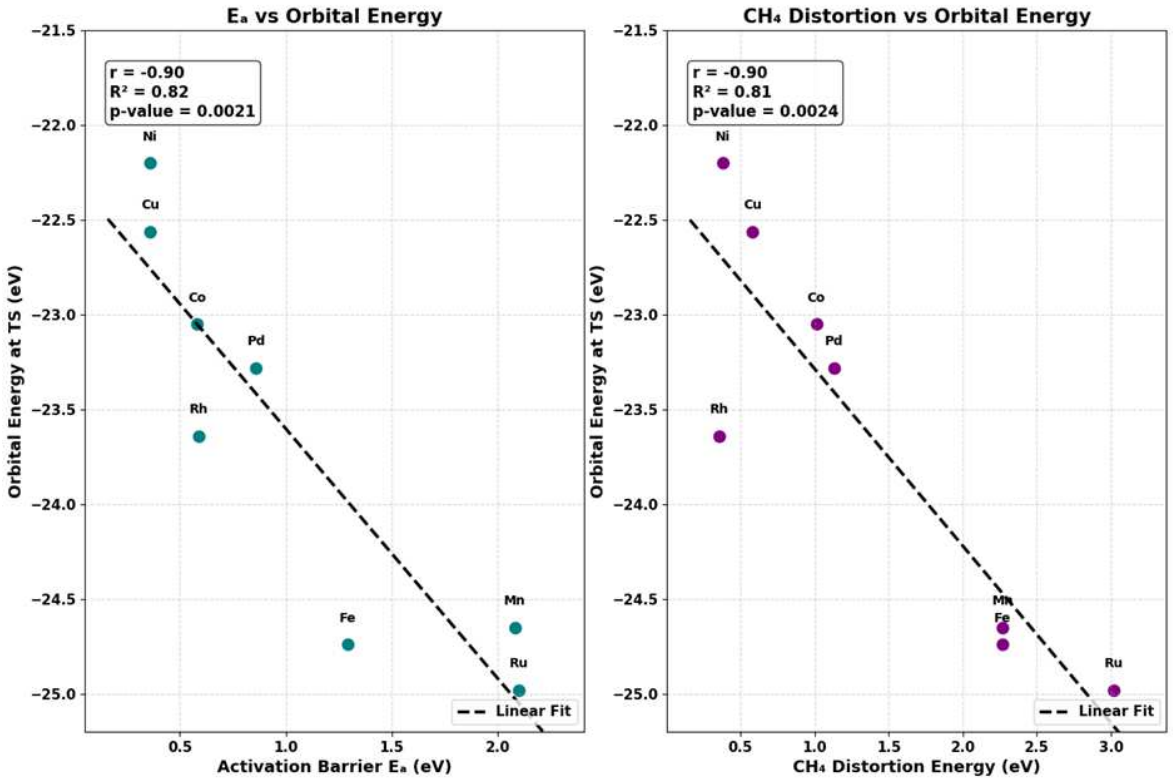


Figure 12: The correlation between the activation barrier/CH_4 distortion energy and the orbital energy at TS

Conclusion

This study presents a comprehensive computational investigation of methane activation over TM@$C_{24}N_{24}$ SACs using a combination of DIAS, QTAIM, and IBO analysis. The findings show that the geometric distortion of methane at the transition state is the main factor controlling the activation barrier, with systems requiring less CH_4 distortion showing much lower energy barriers and increased catalytic reactivity. Catalysts that promote early transition states with minimal structural reorganization are more effective at facilitating C–H bond breakage, as demonstrated by the strong correlation between distortion energy and the activation barrier ($r = 0.94$, $p < 0.05$). The second most crucial descriptor was the transition-state orbital energy ($r = –0.90$, $p < 0.005$), with lower activation energies and better electronic rearrangement associated with more negative orbital energies – Figure 12. These results show that geometric and electronic variables jointly control methane activation. Effective C–H bond destabilization is more critical than early O–H bond creation, as demonstrated by QTAIM analysis, which also revealed that low energy barriers are linked to advantageous electron density distributions and covalent bonding properties at the C–H and O–H bond critical points. Although structurally significant, the TM–O interaction has a secondary effect on reactivity.

This confirms that the conversion of the σ(C–H) orbital into a developing O–H bond, and that catalysts with accessible transition-state orbital energies enable more effective hydrogen atom abstraction. IBO analysis consistently offers electronic insight into the C–H bond cleavage mechanism. A significant interaction between favourable orbital energies and minimal methane distortion can explain the higher performance of some catalysts.

$Ni@C_{24}N_{24}$ and $Cu@C_{24}N_{24}$ exhibit the lowest activation barriers, minimal methane distortion, minimal electronic rearrangement, and electron sharing, making them the most promising single-atom catalysts among the systems examined in this work. In addition to offering practical guidelines for the logical design of next-generation single-atom catalysts for low-barrier methane-to-methanol conversion, this study demonstrates that a combined geometric–electronic descriptor framework is crucial for understanding and predicting the catalytic activity of methane oxidation SACs.

Acknowledgements

The authors would also like to acknowledge the Centre for High-Performance Computing (CHPC), South Africa for providing computational resources and software for this project.

Funding Declaration

Research reported in this work was supported by the University of Johannesburg, Research Centre for Synthesis and Catalysis.

Reference

(1) programme, U. e. What's the deal with methane*?* 2022. unep.org/news-and-stories/video/whats-deal-methane. (accessed:26/04/2024).
(2) Mukona Kune, T. G. Investigating the Environmental and Economic Benefit of Waste to Energy Project: a Case Study of Methane Gas at the Thohoyandou Landfill Site. *Real Corp* **2023**, 445-451.
(3) Duma, Z. The case of green methanol in South Africa; Science and Innovation Republic of South Africa, 2023.
(4) Donghyun Park, J. L. Biological conversion of methane to methanol. *Korean J. Chem. Eng* **2013**, *30*(5). DOI: 10.1007/s11814-013-0060-5.
(5) ChemAnalyst. Decode the Future of Methanol; 2023. chemanalyst.com/industry-report/south-africa-methanol-market-211.
(6) Chris Chatterton, C. Methanol: Recent Developments as a CLEAN Fuel; 2018.
(7) team, S. I. SGS-Inspire-Methanol-Properties-and-Uses; 2020.
(8) Vanessa B. Vilela, F. F.-F., Marlu C. Steil, Vivian V. Thyssen, Daniel Z. de Florio, Andre S. Ferlauto, Fabio C. Fonseca. Conversion of methane into value-added products in catalytic-assisted solid oxide fuel cell. *J. Power Sources* **2025**, *656*, 238083(238081-238013). DOI: 10.1016/j.jpowsour.2025.238083.
(9) Solutions, C. f. C. a. E. *Leveraging Natural Gas to Reduce Greenhouse Gas Emissions*; 2013. www.c2es.org/document/leveraging-natural-gas-to-reduce-greenhouse-gas-emissions.
(10) Xiao, P.; Wang, Y.; Lu, Y.; Nakamura, K.; Ozawa, N.; Kubo, M.; Gies, H.; Yokoi, T. Direct Oxidation of Methane to Methanol over Transition-Metal-Free Ferrierite Zeolite Catalysts. *J. Am Chem Soc* **2024**, *146* (14), 10014-10022. DOI: 10.1021/jacs.4c00646.
(11) Oleg A. Mironov, S. M. B., Michael M. Konnick, Brian G. Hashiguchi, Vadim R. Ziatdinov,; William A. Goddard, M. r. A., and Roy A. Periana. Using Reduced Catalysts for Oxidation Reactions: Mechanistic

Studies of the “Periana-Catalytica” System for CH_4 Oxidation. *ACS* **2013**, *135*, 14644-14658. DOI: 10.1021/ja404895z.
(12) Hojin Jeong, S. S., and Hyunjoo Lee. Heterogeneous Atomic Catalysts Overcoming the Limitations of Single-Atom Catalyst. *ACS Applied Nano Materials* **2020**, *14* (12), 14355−14374. DOI: 10.1021/acsnano.0c06610.
(13) Min Bum Park, E. D. P., and Wha-Seung Ahn. Recent Progress in Direct Conversion of Methane to Methanol Over Copper-Exchanged Zeolites. *Front. Chem* **2019**, *7*, 1-7.
DOI: 10.3389/fchem.2019.00514.
(14) Seyed Alireza Vali, A. A. M., Javier Moral-Vico, Xavier Font, and Antoni Sanchez. Recent Advances in the Catalytic Conversion of Methane to Methanol: From the Challenges of Traditional Catalysts to the Use of Nanomaterials and Metal-Organic Frameworks. J. *Nanomater* **2023**, *13*, 1-24.DOI: 10.3390/nano13202754.
(15) Raimund Horn, a. R. S. Methane Activation by Heterogeneous Catalysis. *Catal Lett* **2015**, *145*, 23-39. DOI: 10.1007/s10562-014-1417-z.
(16) Dummer, N. F.; Willock, D. J.; He, Q.; Howard, M. J.; Lewis, R. J.; Qi, G.; Taylor, S. H.; Xu, J.; Bethell, D.; Kiely, C. J.; Hutchings, G. J. Methane Oxidation to Methanol. *Chem. Rev* **2023**, *123* (9), 6359-6411. DOI: 10.1021/acs.chemrev.2c00439.
(17) Jamie H. Docherty, T. M. L., Gillian Mcarthur, Michael T. Findlay, Pablo Domingo-Legarda,; Jacob Kenyon, S. C., and Igor Larrosa. Transition-Metal-Catalyzed C−H Bond Activation for the Formation of C−C Bonds in Complex Molecules. *Chem. Rev* **2023**, *123*, 7692-7760. DOI: 10.1021/acs.chemrev.2c00888.
(18) Zouhair Boukha, B. d. R., Juan R. González-Velasco, José I. Gutiérrez-Ortiz, and Rubén López-Fonseca. Comparative Study of the Efficiency of Different Noble Metals Supported on Hydroxyapatite in the Catalytic Lean Methane Oxidation under Realistic Conditions. *Mater. Horiz* **2021**, *14*, 3612. DOI: 10.3390/ma14133612.
(19) Bartholomew, M. D. A. a. C. H. Heterogeneous Catalyst Deactivation and Regeneration: A Review. *Catalysts* **2015**, *5*, 145-269. DOI: 10.3390/catal5010145.
(20) Freakley, S. J.; Dimitratos, N.; Willock, D. J.; Taylor, S. H.; Kiely, C. J.; Hutchings, G. J. Methane Oxidation to Methanol in Water. *Acc. Chem Res* **2021**, *54* (11), 2614-2623.
DOI: 10.1021/acs.accounts.1c00129.
(21) Junjie Li, Q. G., Hong Wu, Wei Liu, Zhihu Sun, Xuxu Ye, Xusheng Zheng, Haibin Pan, Junfa Zhu, Si Chen, Wenhua Zhang, Shiqiang Wei, and Junling Lu. Highly Active and Stable Metal Single-Atom Catalysts Achieved by Strong Electronic Metal−Support Interactions. *ACS* **2019**, *141*, 14515-14519. DOI: 10.1021/jacs.9b06482.
(22) XIAO-FENG YANG, A. W., BOTAO QIAO, JUN LI, JINGYUE LIU, AND TAO ZHANG. Single-Atom Catalysts: A New Frontier in Heterogeneous Catalysis. *Acc Chem Res* **2013**, *46* (8), 1740–1748. DOI: 10.1021/ar300361m.
(23) Prajapati, A.; Collins, B. A.; Goodpaster, J. D.; Singh, M. R. Fundamental insight into electrochemical oxidation of methane towards methanol on transition metal oxides. *Proc Natl Acad Sci U S A* **2021**, *118* (8). DOI: 10.1073/pnas.2023233118.
(24) Srinivasu, K.; Ghosh, S. K. Transition Metal Decorated Porphyrin-like Porous Fullerene: Promising Materials for Molecular Hydrogen Adsorption. *J. Phys. Chem C* **2012**, *116* (48), 25184-25189. DOI: 10.1021/jp3047517.
(25) Modak, B.; Srinivasu, K.; Ghosh, S. K. Exploring metal decorated Porphyrin-like Porous Fullerene as catalyst for oxygen reduction reaction: A DFT study. *Int. J. Hydrog. Energy* **2017**, *42* (4), 2278-2287. DOI: 10.1016/j.ijhydene.2016.12.017.
(26) Mousavian, P.; Esrafili, M. D. Methane oxidation into methanol catalyzed by TM-anchored $C_{24}N_{24}$ nanoclusters (TM = Fe, Co and Ni): A DFT study. *Inorg. Chem. Commun* **2020**, *122*. DOI: 10.1016/j.inoche.2020.108317.

(27) Zhang, S.; Lv, X.; Wang, J.; Wang, T.; Shan, J. Catalytic oxidation of CH_4 into CH_3OH using $C_{24}N_{24}$-supported single-atom catalyst. *J. Mol. Model* **2021**, *27* (12), 346(341-348). DOI: 10.1007/s00894-021-04971-2.
(28) Bickelhaupt, F. M. Understanding reactivity with Kohn-Sham molecular orbital theory: E2-S_N2 mechanistic spectrum and other concepts. *Wiley* **1999**, *20* (1), 114-128. DOI: 10.1002/(sici)1096-987x(19990115)20.
(29) F. Matthias Bickelhaupt, a. K. N. H. Analyzing Reaction Rates with the Distortion/Interaction-Activation Strain Model. *Angew. Chem. Int. Ed.* **2017**, *56*, 10070-10086. DOI: 10.1002/anie.201701486.
(30) Bader, R. F. W. *QTAIM:* quantum theory of atoms in molecules. *Struct.dyn.* 2009. (accessed: 18/09/2025).
(31) Johannes E. M. N. Klein, G. K., Burkhard Miehlich, Johannes K stner, and Bernd Plietker. Fe or Fe NO Catalysis? A Quantum Chemical Investigation of the $[Fe(CO)_3(NO)]$-Catalyzed Cloke–Wilson Rearrangement. *Chem. Eur. J.* **2014**, *20*, 7254-7257. DOI: 10.1002/chem.201402716.
(32) Lando P. Wolters, W.-J. v. Z., and F. Matthias Bickelhaupt. New Concepts for Designing d10-M(L)n Catalysts: d Regime, s Regime and Intrinsic Bite-Angle Flexibility. *Chem. Eur. J.* **2014**, *10*, 11370-11381. DOI: 10.1002/chem.201403237.
(33) BIOVIA, D. S. BIOVIA MATERIALS STUDIO DMOL3 DATASHEET. 2017.
(34) Perdew, J. P. Density-functional approximation for the correlation energy of the inhomogeneous electron gas. *Phys. Rev. B.* **1986**, *33* (12), 8822-8824.
(35) John P. Perdew, K. B., Matthias Ernzerhof. Generalized Gradient Approximation Made Simple. *The APS* **1996**, *77* (18), 3865-3868. DOI: 0031-9007y96y77(18)y3865(4)$10.00.
(36) Kohlenforschung, M.-P.-I. f. ORCA Manual 6.0.0. 2024.
(37) Boyd, K. Finding the Transition State of a Chemical Reaction of Interest Using Avogadro, ORCA, and IboView. 2020.
(38) Bursch, M.; Mewes, J. M.; Hansen, A.; Grimme, S. Best-Practice DFT Protocols for Basic Molecular Computational Chemistry. *Angew. Chem. Int. Ed. Engl.* **2022**, *61* (42), e202205735. DOI: 10.1002/anie.202205735.

Supplementary Files

This is a list of supplementary files associated with this preprint. Click to download.

- SupportingInformation.docx